International Journal of Fracture **108:** 165–191, 2001.

Numerical modelling of fracture initiation and propagation in biaxial tests on rock samples

B. VAN DE STEEN[1], A. VERVOORT[1] and J.A.L. NAPIER[2]
[1]*Department of Civil Engineering, KULeuven, W. de Croylaan 2, 3001 Leuven, Belgium (Author for correspondence; e-mail: bart.vandesteen@bwk.kuleuven.ac.be)*
[2]*CSIR, Mining Technology, Johannesburg, South Africa*

Received 16 March 2000; accepted in revised form 13 September 2000

Abstract. A two-dimensional boundary element code, based on the displacement discontinuity method is used to simulate a confined compression test. The method takes account of the granular nature of the rock and of the presence of pre-existing defects. Fracture propagation is thought to depend, amongst other factors, on the crack orientation, the residual friction angle, the dilation angle, and the confining pressure. To obtain a more precise understanding of the influence of these properties on the crack growth process, their influence on the normal stress and the excess shear stress on potential fracture planes ahead of the crack tip is investigated for a single crack configuration. The orientation of the potential fracture planes proves to be the most important parameter determining fracture growth. A series of numerical experiments is carried out to determine the influence of the tessellation pattern used to represent the granular nature of the rock. Both the influence of the type of tessellation and the tessellation density are evaluated, and reasons for the differences in behaviour are presented. The results of the simulations with the Delaunay and a Voronoi tessellation with internal fracture paths compare well with the fracture pattern obtained in laboratory tests. The pre-peak non-linearity in the stress-strain response obtained with the Voronoi tessellation and the post-peak strain softening obtained with the Delaunay tessellation are combined in one model. For that purpose, a Voronoi tessellation with internal fracture paths is used, whereby the properties of the elements of the polygons and of the internal fracture paths are assigned different values. The role that is played by shear failure and the influence of dilation on the localisation process is determined by means of some further numerical experiments. It is shown that at the scale, at which the material is modelled, shear failure is required for a shear band to develop.

Key words: Boundary elements, brittle rock, Delaunay, displacement discontinuity, Voronoi.

1. Introduction

Stress levels around excavations in mining, petroleum or civil engineering applications regularly exceed the strength of the material, resulting in fracturing around the workings. An in-depth evaluation of the rock mass behaviour surrounding these excavations requires a fundamental understanding of the fracture initiation and growth processes in the rock. Therefore, fundamental research is focussed on aspects of the onset and propagation of fractures. Laboratory testing and numerical modelling studies are hereby carried out to provide a better understanding of the nature of failure, the mechanisms involved in crack initiation and the processes controlling damage evolution and localisation.

The study presented here concentrates on granular rocks with a brittle nature. The research aims at clarifying some of the fundamental processes that may play a role in the fracture initiation in rocks and the development of the macroscopic fracture pattern observed in laboratory testing of crinoidal limestone. While interatomic breakage processes must lie at the

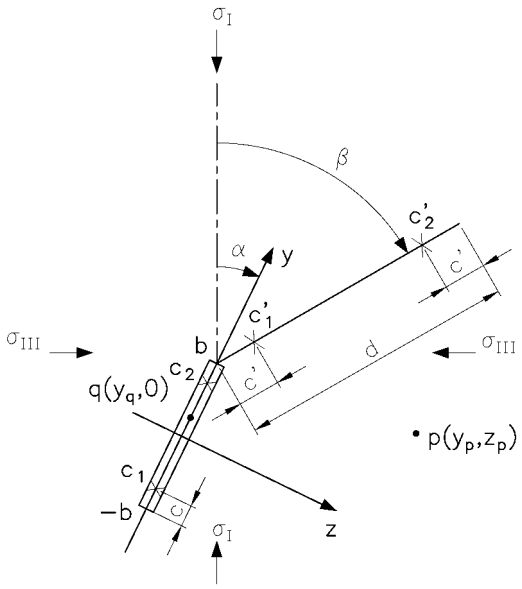

Figure 1. Crack-element configuration with local coordinate system.

basis of the fracturing process (Lawn, 1993), no processes at the atomic level are considered here. It is assumed that the development of macroscopic fractures, which forms the subject of this paper, is in the first place the result of processes on the micro-scale. Therefore, the present research considers the processes at the scale of millimetres and fractions of millimetres, which corresponds to the larger grain size, and is approximately an order of magnitude larger than the average grain size. It is recognised that the stress distribution at this level is inhomogeneous because of the presence of defects in both the grains and in the matrix material. These defects or weaknesses embrace weakly cemented grain boundaries, inclusions, pores, pre-existing cracks etc. The rock type considered in this study, a crinoidal limestone, has a very low porosity ($<$0.70%), and the dominant defects and weaknesses form features with a low width to length ratio. Attention is focussed therefore on crack-like defects. Although the above-mentioned problems are three-dimensional, a firm understanding of the issues in two dimensions should precede any further analysis. In this paper, a 2-D version of a boundary element program is utilised for the simulations providing a solution for the plain strain problem.

The main features of the modelling approach, are the explicit fracture modelling, the recognition of the granular composition of the material and the introduction into the models of randomly placed flaws that serve as fracture initiators. In this paper, it is shown how a random arrangement of growing cracks in confined compression tests at low confining pressures may result in a localisation into a shear band. The influence is further discussed of how some of the model parameters may influence the macroscopic response.

2. Explicit fracture modelling

The two-dimensional boundary element code DIGS (Discontinuity Interaction and Growth Simulation) allows for an explicit fracture modelling (Napier, 1990; Napier and Hildyard, 1992; Napier and Pierce, 1995; Malan and Napier, 1995; Kuijpers and Napier, 1996, Napier

et al., 1997; Napier and Malan, 1997). If the initial failure process can be represented by small strain dislocations, and if dynamic effects can be discarded, the cracks can be modelled as displacement discontinuities. The displacement discontinuity boundary element method (Crouch and Starfield, 1983) forms the basis for the code. In an elastic solid, the displacements are assumed continuous, except over the discontinuity elements. Over straight-line elements with normal vector components n_y and n_z, centred on the y-axis of a local coordinate system y-z (Figure 1), the local displacement discontinuity components are defined as:

$$D_i(y_q) = u_i(y_q, 0_-) - u_i(y_q, 0_+) \qquad i = y, z; -b \leq y_q \leq b, \tag{1}$$

where $z = 0_+$ the positive side and $z = 0-$ the negative side of the discontinuity. The displacements and the stresses over an element are represented in a number of collocation points. In the original displacement discontinuity formulation, the displacement discontinuities over the element were constant and the displacements and the stresses at a single mid-element collocation point were assumed to adequately represent the stresses and displacements over the face of a discontinuity. More accurate results can be obtained with linear, quadratic or higher order elements, with respectively 2, 3 or more collocation points at which the displacements and stresses are determined such that the boundary conditions are satisfied (Crawford and Curran, 1982). If the displacement discontinuity varies linearly over a discontinuity element with length 2b, as is the case in DIGS, (1) becomes:

$$D_i(y_q) = \alpha_i + \beta_i y_q \qquad \alpha_i, \beta_i \text{ constants}. \tag{2}$$

The contribution of an element to the total stress components at a point $p(y_p, z_p)$ in isotropic elastic material with Young's modulus E and Poisson's ratio v is given by[1]:

$$\begin{bmatrix} \sigma_{yy}(y_p, z_p) \\ \sigma_{yz}(y_p, z_p) \\ \sigma_{zz}(y_p, z_p) \end{bmatrix} = \frac{E}{8\pi(1-v^2)} \int_{-b}^{b} \begin{bmatrix} -\Psi_{,zzzz} & \Psi_{,yzzz} - \Psi_{,yyzz} \\ \Psi_{,yzzz} - \Psi_{,yyzz} & \Psi_{,zzzz} \\ -\Psi_{,yyzz} & \Psi_{,yyyz} - \Psi_{,yyyy} \end{bmatrix} \begin{bmatrix} D_y(y_q) n_y \\ D_y(y_q) n_z + D_z(y_q) n_y \\ D_z(y_q) n_z \end{bmatrix} \mathrm{d}y_q \tag{3}$$

For two-dimensional plane strain problems:

$$\Psi = \frac{1}{2}(r^2 - r^2 \log r^2) \quad \text{and} \quad r^2 = (y_p - Y_q)^2 + z_p^2.$$

The normal stress on the y-axis of the local coordinate system is given by:

$$\sigma_{zz}(y, 0) = \frac{E}{8\pi(1-v^2)} \left[2(\alpha_z + \beta_z y) \left(\frac{1}{y+b} - \frac{1}{y-b} \right) + \beta_z \log \left(\frac{y+b}{y-b} \right)^2 \right]. \tag{4}$$

It is obvious from (4) that the stress values for $y = \pm b$ become singular. This requires that the collocation points at which the stresses and displacements are determined have to be placed in the interior of the elements. If it is assumed that the element stresses may reasonably be represented by a polynomial, the stress distribution along an element is best represented by the stresses at collocation points located at the Gauss-Chebyshev points (Crawford and Curran, 1982).

$$y_i = \cos(2i - 1)\frac{\pi}{2n} \qquad i = 1, 2, \ldots, n. \tag{5}$$

[1]The comma behind Ψ denotes derivatives (that is $\Psi_{,yyzz} = \partial^4 \psi / \partial y^2 \partial z^2$)

From (5) it follows that for the linear variation elements ($n = 2$), the points should be situated at $y = \pm(\sqrt{2}/2)b$ from the centre of the element, such that $c = \pm(1 - \sqrt{2}/2)b$ (Figure 1). Napier (1990) provides additional arguments relating to the opening displacement of a single element to situate the collocation points at the above-mentioned distance for linear variation elements.

The total stress values at the point p are given by summing the contributions (3) from each defined discontinuity element that is used to represent both the excavation or sample geometry and the cracks and fractures within the material. The shear and normal traction at a collocation point $y = y_c$ within a given element are given by:

$$\begin{cases} \sigma_{yz} = K_0 D_y(y_c) + E_{yz}(y_c), \\ \sigma_{zz} = K_0 D_z(y_c) + E_{zz}(y_c), \end{cases} \tag{6}$$

where K_0 is the self-effect influence coefficient, and E_{yz} and E_{zz} are the so called external influences. The external influences are built up of the influence of the other collocation point of the same element at $y = -y_c$ through the influence coefficient K, and of the primitive stresses, and the stress induced by all other mobilised displacement discontinuities, whose influence at $y = y_c$ is given by E'_{yz} and E'_{zz}.

$$\begin{cases} E_{yz}(y_c) = K D_y(-y_c) + E'_{yz}(y_c), \\ E_{zz}(y_c) = K D_z(-y_c) + E'_{zz}(y_c), \end{cases} \tag{7}$$

From (6), the values of D_y and D_z are determined, using an iterative technique. In the case of frictional sliding, (6) is complemented with the equilibrium condition:

$$e\sigma_{yz}(y_c, 0) = S_0 - \tan\varphi_r \sigma_{zz}(y_c, 0),$$

where S_0 is the residual cohesion, φ_r is the residual friction angle and $e = +1$ if $E_{yz} < 0$ and $e = -1$ if $E_{yz} > 0$. In what follows, S_0 is taken zero. Unless D_z is determined by tensile stresses, it is assumed that

$$D_z(y_c) = -\tan\psi |D_y(y_c)|,$$

where ψ is the dilation angle.

Fractures are often seen to follow preferred directions such as grain boundaries and cleavage planes (Peng and Johnson, 1972; Kranz, 1979a, b; Wong, 1982; Chen et al., 1999). Studies on untested rock samples using scanning electron microscopy and optical microscopy techniques also indicate that untested rock samples contain a high number of pre-existing defects. For granitic rocks, the following data were published: crack densities of 0.672 cracks per mm^2 sample (Peng and Johnson, 1972); a crack length density of 3.56 mm per mm^2 sample (Chen et al., 1999) and crack/pore intersection rate of 1.4 cracks per mm traverse with an average crack length of 0.054 mm per crack (Kranz, 1979a). Studies of other rock types also indicate the abundance of pre-existing defects (Bathurst, 1991; Kožušnikova and Marečkova, 1999). Since it would be impractical to model all these effects individually, equivalent structures that represent the effect of the defects have to be devised. These equivalent structures are termed flaws, and are distributed randomly over the sample. The region of interest may be overlaid with a random grid defining the possible discontinuity elements. The random grid defines the potential fracture paths, thereby simulating the granular texture and the internal structure of the composing minerals. A number of strength properties and post-failure characteristics are associated with each grid element. Assigning reduced strength parameters to a random set of

elements allows for the introduction of the flaws. The stresses at the collocation points of the grid elements are evaluated against the specified failure criterion. The element or elements, for which the failure criterion is exceeded, are retained for activation and one or more can be added to the list of discontinuity elements. In the case of a Coulomb failure criterion, an internal friction angle φ_i is used as long as an element has not failed to determine the resistance against shear failure. After failure, the resistance against sliding is determined by the residual friction angle φ_r. Individual discontinuity elements are also referred to as cracks. The term fractures is used for a number of cracks connected to each other. The initial displacement discontinuities D_y and D_z of all the grid elements, no matter whether they have reduced properties or not, is equal to zero.

The random grid is generated by a Delaunay–Voronoi generator: after generating a random set of points (= sites) in the area to be meshed, triangles (Delaunay) or polygons (Voronoi) are constructed (Finney, 1979, Malan and Napier, 1995; Napier and Peirce, 1995). Additional edges can be obtained in the Voronoi tessellation, by connecting the geometric centre of the Voronoi polygons with the vertices of the polygons. These last elements are further referred to as the internal fracture paths, while the points in which two or more elements are joined are referred to as nodes. An example of each of the tessellations is given in the discussion of the numerical simulations (see further: Figure 6a: Delaunay; Figure 8a Voronoi and Figure 10a Voronoi with internal fracture paths).

To obtain an indication of possible localisation, the second invariant of the deviatoric part of the inelastic strain (Sellers and Napier, 1997) or the octahedral inelastic shear strain γ can be considered. The octahedral shear strain γ_{oct} is related to the second invariant of the deviatoric strain tensor J_2' (Chen and Han, 1988) and provides a measure for the shear deformation.

$$\gamma_{\text{oct}} = 2\sqrt{\frac{2}{3}J_2'}, \tag{8}$$

$$J_2' = \tfrac{1}{6}[(\varepsilon_{xx} - \varepsilon_{yy})^2 + (\varepsilon_{yy} - \varepsilon_{zz})^2 + (\varepsilon_{zz} - \varepsilon_{xx})^2] + \varepsilon_{xy}^2 + \varepsilon_{yz}^2 + \varepsilon_{zx}^2. \tag{9}$$

For the plastic strain in plane strain, the total strain components are substituted by the average inelastic strain components, and (9) becomes:

$$J_2'^p = \tfrac{1}{6}[(\overline{\varepsilon_{xx}^p} - \overline{\varepsilon_{yy}^p})^2 + (\overline{\varepsilon_{yy}^p}^2 + \overline{\varepsilon_{zz}^p}^2] + \overline{\varepsilon_{yz}^p}^2. \tag{10}$$

The average inelastic strain in an area A containing discontinuity elements with a total crack length C is given by (Sellers and Napier, 1997):

$$\overline{\varepsilon_{ij}^p} = \frac{1}{2A}\int_C (D_i n_j + D_j n_i)\mathrm{d}S. \tag{11}$$

3. Stress distribution around individual cracks

In the further discussion, either a Rankine or a Coulomb failure criterion is considered. Failure depends on either the normal tensile stress σ_{zz} or on the excess shear stress (ESS or net driving shear stress) on an element (in local co-ordinates ESS = $|\sigma_{yz}|$ - tgφ_{i} σ_{zz}, where φ_{i} is the internal friction angle of the material). Fractures are built up of a number of activated elements joined

end to end. The fracture length L_f is expressed as the sum of the individual lengths l_i that make up the fracture. Crack growth occurs when either the normal stress or the ESS at the collocation point of an element joined to an activated crack satisfies the failure criterion. The direction in which the normal stress and the ESS have to be evaluated is determined by the orientation of the element. The element orientation is expressed as the angle β between the element direction and the major principal stress direction (Figure 1).

To evaluate the influence of a number of parameters on the fracturing process, a parametric study is carried out. To this effect, a plain strain analysis is carried out of the stress field around a single displacement discontinuity (also called crack) with length $2b$, placed in a stress field defined by the far field stresses $P_1 = \sigma_I$ and $P_2 = \sigma_{III}$. To evaluate the impact of the different parameters on the crack growth, an element with length d and orientation β, joined to one of the crack tips is considered as a function of the element orientation α. The normal stress and the ESS are then calculated in the collocation point closest to the crack tip. The influence of the following parameters is determined:

- the crack angle α,
- the element angle β,
- the residual friction angle φ_r,
- the dilation angle ψ,
- the confining stress P_2,

The configuration that serves as a base for the parametric study consists of a single displacement discontinuity element that makes an angle α of 35° with the major principal stress σ_I (Figure 1). The applied compressive stresses are equal to $P_1 = \sigma_I = 10$ MPa, and $P_2 = \sigma_{III} = 1$ MPa[2]. The dilation angle ψ is equal to 15° and the residual friction angle is equal to 20°. The ESS is calculated with an internal friction angle $\varphi_i = 40°$. The crack length 2b is equal to the length d of the neighbouring elements. Hence, the distance from the crack tip to the first collocation point c'_1 is equal to:

$$c' = c = \frac{1}{2}\left(1 - \frac{\sqrt{2}}{2}\right) d = \frac{1}{2}\left(1 - \frac{\sqrt{2}}{2}\right) 2b.$$

The discussion of the parameter study is restricted to the influence of the crack angle α on the ESS and on the normal stress. For the other parameters, only the main results and conclusions are given in here.

In a compressive biaxial stress field with $P_1 \neq P_2$, crack sliding can only occur if the crack angle $\alpha < 90° - \varphi_r$. The stress field in a specimen containing a single crack with $\alpha > 90° - \varphi_r$ is therefore equivalent to the stress field in a crack free specimen.

The influence of a change in the crack angle α is used to illustrate the major characteristics of the normal stress and the ESS distribution as a function of the element angle β, and to indicate the sensitivity of the results to a change in one of the parameters (Figures 2a and 2b). The curves of the normal stress as a function of the element angle β for a number of different crack orientations α are given in Figure 2a. Save for a crack of 0°, the curves are not symmetric. If the crack orientation α is positive, the minimum normal stress (i.e. either the smallest compressive stress or the highest tensile stress) is recorded for element angles β between 0° and −5° depending on the crack angle α. Since the crack is placed in a uniform stress field, all the curves obtained for negative crack angles α are symmetric to the curves obtained for positive crack angles α.

[2]Henceforth compressive stresses and angles measured in clockwise direction are positive.

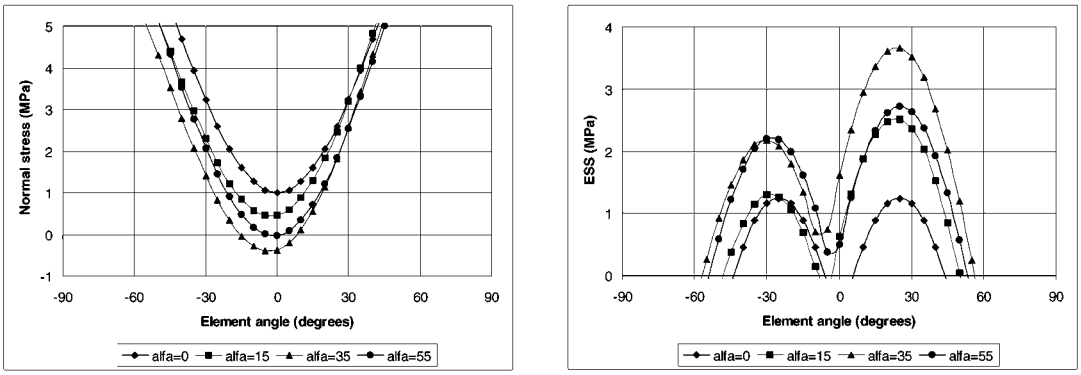

Figure 2. Influence of crack angle α on normal stress (a) and ESS (b) in response to a single displacement discontinuity element ($P_1 = 10$ MPa, $P_2 = 1$ MPa, $\varphi_i = 40°$ $\varphi_r = 20°$, $\psi = 15°$).

The ESS curves (Figure 2b) are characterised by two maxima. The position of these maxima is only marginally affected by a change in element angle. The element angle at which the highest maxima in ESS are recorded is equal to approximately 25° for cracks with an orientation between 0° and 55°. The second maximum in the ESS curves is recorded at $\beta = -25°$ to $-30°$, depending on the crack angle α. It is obvious from Figure 2a and 2b that the element angle β, much more than the crack angle α determines the normal stress and the ESS at an element adjacent to a crack. The influence of the crack angle α cannot be totally dismissed though. Under the circumstances applicable in this example ($P_1/P_2 = 10$; $\varphi_i = 40°$; $\varphi_r = 20°$; $\psi = 15°$), the crack angle should have a value in between 25° and 55° for a limited number of element orientations to be subjected to a tensile stress. Similarly, the maximum ESS attained is largest when the crack has an orientation between 25° and 45°. In their study on wing crack initiation, Li et al. (1998) obtained similar results. Using a mode II fracture criterion, they concluded that the wing cracks are most easily initiated on pre-existing cracks located in the range of $\alpha = 20°$ to $\alpha = 50°$.

A characteristic of the displacement discontinuity method is that, independent of the modelled crack width (which is equal to zero in the work presented here), the applied stress component parallel to the crack does not lead to an induced stress component perpendicular to the crack. Hence, the stress field at the tip of a crack with $\alpha = 0°$ (Figures 2a and 2b) is symmetric with respect to the vertical and it reflects the stress field in a crack free sample.

The curves of the normal stress as a function of the element angle β obtained for a variation in the crack angle α depict the typical characteristics encountered in the normal stress and ESS-curves as a function of the element angle β for the other parameter studies. The single minimum in the normal stress curves in the vicinity of the principal stress direction (0°), and the two maxima in the ESS curves as well as the overriding influence of the element orientation are found back when the influence of the other parameters is studied. The main results of these parameter studies can be summarised as follows:

– The influence of a change in dilation angle or a change in friction angle is limited. A decrease in the residual friction angle and an increase in the dilation angle tend to enhance the stress concentration in the vicinity of the crack tip. This is translated in a lowering of the normal stress and an increase in the ESS for a certain element angle β.
– An increase in the confining pressure invariably shifts the normal stresses at an element to higher values, making tensile failure more and more unlikely and even impossible as

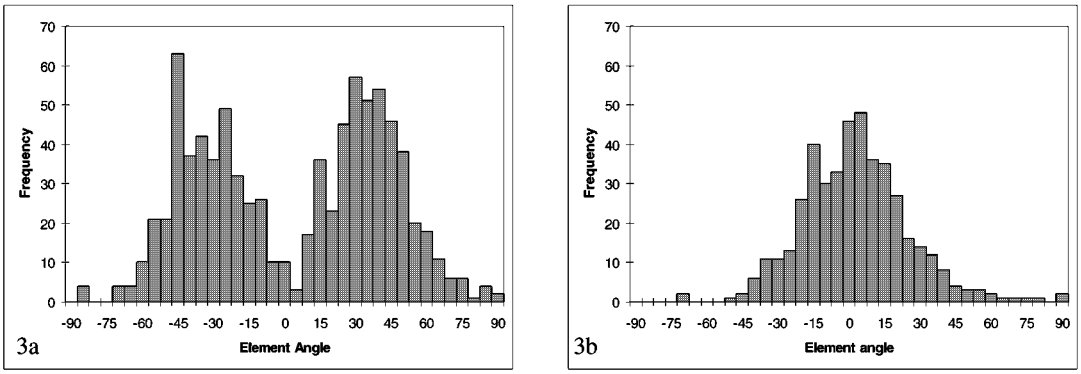

Figure 3. Orientation of the elements activated in shear (a) and activated in tension (b) in a simulation of a biaxial test. The orientation of the 4583 elements activated in sample V2 (see figure 8c) is determined relative to the vertical sample axis.

the normal stress eventually becomes compressive for all element orientations with an increase in the confinement. Similarly, the ESS is decreased considerably by an increase in confining pressure.

It can here be indicated that an increase in the ratio of the crack length to the element length ($2b/d$) has a more pronounced influence on the normal stress and the ESS curves. A discussion of this topic falls however outside the realm of this paper.

For the displacement discontinuity method, it can be concluded that for elements joined to an activated crack that makes a positive angle α with the major principal stress, the elements that make an angle β of approximately 20° to 30° with σ_{I} are subjected to the highest ESS. A second local maximum in the ESS is reached for elements with an orientation β of approximately $-35°$ to $-25°$. The lowest normal stress (i.e., either the smallest compressive stress or the highest tensile stress) at a collocation point is reached for elements with an orientation β of approximately $-5°$ to 0°. The element angles for which these maxima are reached are mainly determined by the direction of the principal stresses. The element angles for which the maxima occur, are not very sensitive to the crack angle, the dilation angle, the residual friction angle or the confinement. A histogram of the element orientation for elements that failed in shear and tension in a numerical simulation of a biaxial test is given in Figure 3. The histogram refers to simulation V2 (see also Figure 8c). The element orientations are expressed with respect to the sample axis, which coincides with the direction of the major principal stress (see Figure 1). The results indicate that the foregoing conclusions, derived in a two-dimensional analysis for a single crack configuration also apply to a multi-crack configuration in a two-dimensional plane strain simulation of a biaxial test.

4. Numerical simulations of the biaxial test

In a polyaxial cell, a true triaxial stress state can be applied: $\sigma_{\mathrm{I}} > \sigma_{\mathrm{II}} > \sigma_{\mathrm{III}}$. The special case in which $\sigma_{\mathrm{I}} > \sigma_{\mathrm{II}} = \sigma_{\mathrm{III}}$ is most commonly used in the laboratory testing of cylindrical rock specimen. The test, known as the triaxial test, is described in detail in most manuals on rock mechanics (Jaeger and Cook, 1979; Brady and Brown, 1993). In the case discussed in this paper, σ_{III} is held constant and σ_{I} is increased while $\varepsilon_{\mathrm{II}}$ (whose direction coincides here with the direction of σ_{II}) $= 0$ (plane strain). This case is here referred to as a biaxial test.

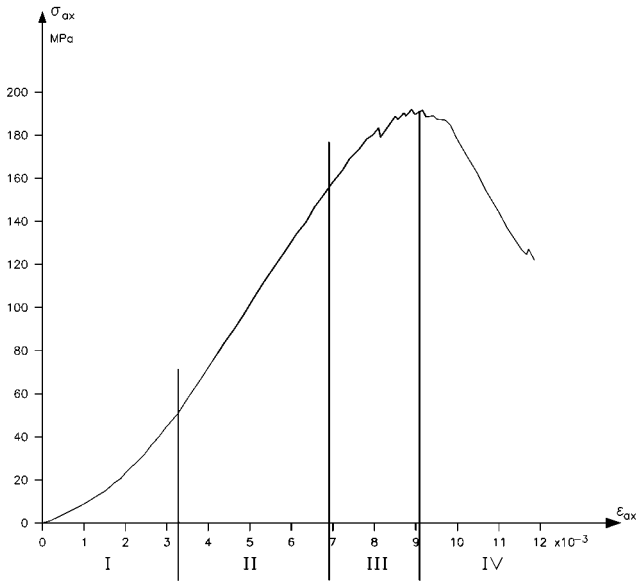

Figure 4. Experimental stress-strain curve of a triaxial test on a crinoidal limestone wit a confining pressure of 10 MPa.

In the failure criterion used (Coulomb with tension cut off) only the major and the minor principal stress play a role. This implies that the fracture pattern obtained in a biaxial test should be comparable to the fracture pattern obtained in a triaxial test. The localisation process can be described as the development of a band inclined at an angle of less than 45° to σ_I in which microfractures coalesce to form a macroscopic shear band. A detailed discussion of the failure mechanism and the stress-strain relationship can be found in Hallbauer et al. (1973) or in Jaeger and Cook (1979). A typical stress-strain curve obtained from a triaxial test with a confining stress of 10 MPa on a crinoidal limestone is given in Figure 4. Four of the five regions that can be associated with the stress-strain relationship for triaxial tests on brittle materials are indicated on Figure 4 (Hallbauer et al. 1973; Jaeger and Cook, 1979). The test depicted in Figure 4 was stopped before region V was reached, in which sliding along macroscopic fracture planes occurs.

In the following sections a number of two-dimensional plane strain numerical simulations of the biaxial test are considered. The main aim is to determine the influence of the mesh size and the tessellation geometry on the simulation results, the dominant failure mode and the role played by dilation. Besides the sample (50 mm × 100 mm), the loading platens were modelled to enable the friction between the platens and the sample to be accounted for. Displacements were applied in steps of 0.025 mm. Unless stated otherwise, the material properties of the elements and the flaws listed in Table 1 are used. The flaws are, as stated previously, structures representing the effect of the defects in the material. Since individual cracks are often bridged by uncracked or healed material (Sprunt and Brace, 1974), the flaws are also given a cohesion and a tension cut off.

4.1. MESH SIZE

To assess the influence of the tessellation pattern and the mesh fineness on the fracture pattern and on the stress-strain behaviour, four simulations with progressively finer meshes are

Table 1. Material properties of elements and flaws used in the simulations.

	Flaws	Elements
Cohesion	25 MPa	80 MPa
Residual cohesion	0 MPa	0 MPa
Unmobilised friction angle	35°	35°
Mobilised friction angle	20°	20°
Dilation angle	15°	15°
Tension cut off	−7 MPa	−35 MPa

	General
Friction platen-sample	20°
Percentage flaws	12.5%
Confining pressure	10 MPa

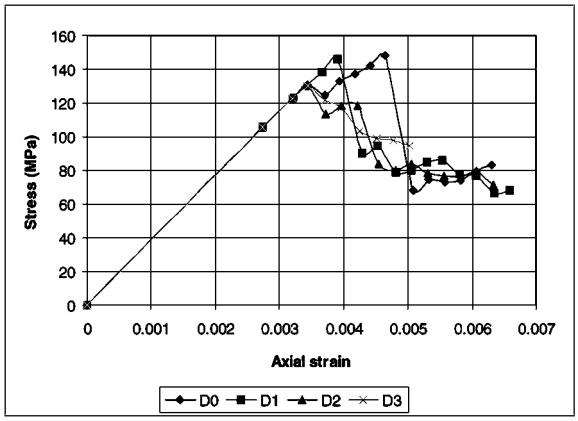

Figure 5. Average axial stress as a function of the average axial strain for the simulation of a biaxial test of a series of Delaunay samples with an increasingly higher tessellation density.

performed per tessellation pattern. The three tessellation patterns that are considered are the Delaunay tessellation, its dual the Voronoi tessellation and a Voronoi tessellation in which additional elements are added. The relation between the tessellation and the fracture pattern is for each tessellation type indicated for the most coarsely meshed sample.

The influence of the tessellation density on the response is evaluated for a series of Delaunay tessellations having 654 elements (D0), 2673 elements (D1), 5199 elements (D2) and 7853 elements (D3), respectively. The stress-strain curves reach in each instance a peak stress (Figure 5). The fracture patterns illustrating the shear banding obtained with the different tessellation densities are shown in Figure 6. As will be discussed further, the octahedral inelastic strain also illustrates the localisation (Figure 11a). In these simulations, attention is focussed on the fracture initiation, fracture growth and localisation process. No attempts were made to model the closure of cracks that may initially be open as described by Walsh (1965a, b). The initial displacement discontinuity D_y and D_z of the flaws are thus equal to zero. Hence, region I (Figure 4) is not present on any of the simulated stress-strain curves (e.g., Figure 5).

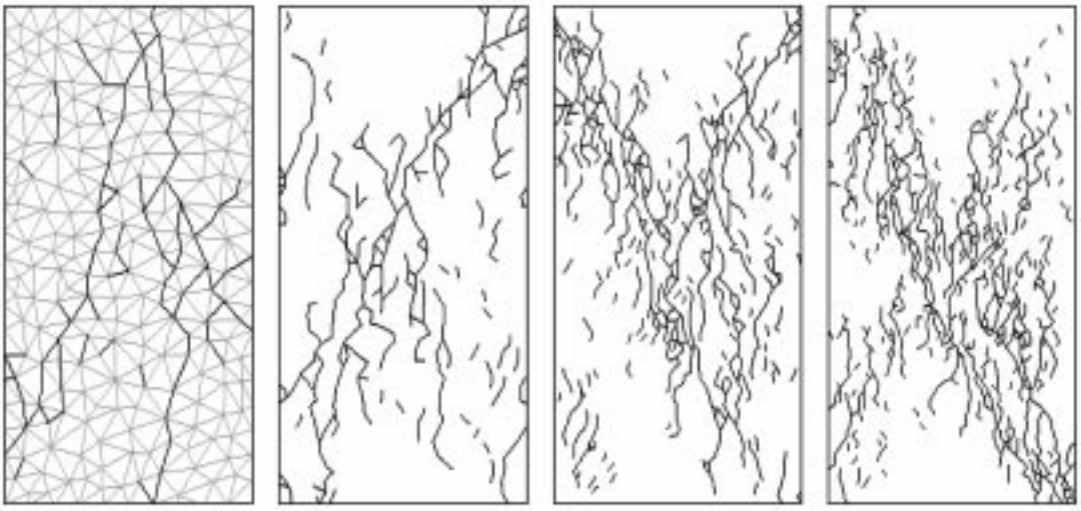

Figure 6. Fracture pattern obtained with an increasingly finer Delaunay tessellation at $\varepsilon = 0.005$ in the simulation of a biaxial test. The fracture pattern of D0 is overlaid on the tessellation pattern.

The regions II, III and IV on the other hand can be recognised in several of the stress-strain curves. In the linear-elastic part (region II) of the simulation, no elements are activated. The non-linear part indicated as region III in Figure 4 commences in the simulations when the first flaws are activated, and ends as the peak stress is reached ($\Delta\sigma_{ax}/\Delta\varepsilon_{ax} > 0$). In region IV, a stress decrease is registered with increasing axial strain ($\Delta\sigma_{ax}/\Delta\varepsilon_{ax} < 0$). In this stage, small oscillations in the stress level often occur in the simulations. In most simulations, region V is attained as well. A stage of continuous deformation is reached if one or more shear planes that affect the whole sample have been generated, allowing a nearly unlimited axial movement. The stress changes with increasing axial strain then remain small. If the shear plane that has been formed affects only part of the sample, a saw tooth pattern is obtained (Figure 5, curve D3). The drop in the average stress remains then limited since the stress is not relieved over the full width of the sample. Further displacements cause again an increase in the load, until a second or third shear plane is formed that allows another part of the sample to shed part of its load.

The step in which the main stress drop is registered is the step in which a fracture is formed that extends from the side of the sample to either the other side of the sample or to the bottom or the top of the sample. The orientation of this fracture has to be such that sliding can occur to relieve the stress in part of the sample. Since the displacement discontinuity at the free boundary is not restricted, the resulting axial movement of the part of the sample influenced by the fracture causes a decrease of the average axial stress. The particular position of the flaws in the mesh as well as the position of the elements influence the size of the stress drop and the stress at which this stress relieving fracture reaches the boundary. For the same flaw and element properties, the brittleness characterised by the main stress drop, decreases in general with an increase in the tessellation density (Figure 5). It should be stressed though that the randomness in the mesh and flaw generation introduces a spread in the results (D0 and D0c, Table 2). The spread increases as the number of elements per sample decreases. A more brittle behaviour can be obtained with the same mesh, by bringing the strength properties of the flaws

Table 2. Element, flaw and mesh properties used to investigate the influence of the mesh randomness and the flaw and element properties. Two different meshes A and B were used.

	D0	D0b	D0c	D0d
	Mesh A		Mesh B	
Ratio average element length to sample width	0.1050		0.1050	
Standard deviation of ratio element length to sample width	0.0259		0.0258	
Number of elements	654		651	
Main stress drop	80 MPa	37 MPa	21 MPa	57 MPa
Cohesion intact elements	80 MPa	80 MPa	80 MPa	60 MPa
Tension cut off intact elements	−35 MPa	−35 MPa	−35 MPa	−30 MPa
Cohesion flaws	25 MPa	25 MPa	25 MPa	30 MPa
Percentage flaws	12.5%	25%	12.5%	12.5%
Tension cut off flaws	−7 MPa	−7 MPa	−7 MPa	−8 MPa

and the intact elements closer together (D0c to D0d, Table 2). Delaunay samples without flaws therefore display a very brittle behaviour (Napier and Peirce, 1995). To obtain a more plastic behaviour, it may be necessary to adjust the flaw density as well (D0 to D0b, Table 2). The brittleness of the simulated biaxial tests is also function of the modelled friction between the sample and the platens. Repeating simulation D2 with a frictionless contact between platens and sample renders a stress-strain curve that displays a considerable stress.

The tessellation density has an influence also on the formation of shear bands or shear planes, which are formed in each of the samples. In samples with a coarse mesh, the shear planes along which the major sliding occurs consists of a limited number of elements (15 and 21 in D0) and is easily discernible in the fracture pattern (Figure 6a). The fracture path is the result of a single crack that grows steadily into the final shear plane. Existing fractures and cracks can hereby be included, but there is nothing like the coalescence of a number of small fractures aligned in a certain pattern. In the finely meshed samples on the other hand the localisation is attributed to the coalescence of cracks and small fractures, aligned in what could be described as a shear band.

The number of elements in the simulations of the samples meshed with a Voronoi tessellation was increased from 608 (V0) to 2427 (V1) to 4583 (V2) and to 6924 (V3). To generate the Voronoi polygons, the same geometric centres used to generate the Delaunay polygons were utilised. In the simulated biaxial tests cracking and fracturing is, with the exception of V0, quite extensive (Figure 8). The stress-strain curves (Figure 7) are slightly non-linear, indicating a certain plasticity; but no peak strength or strain softening stage is reached. There is also no percolation from the top or the bottom to one of the sides in any of the four samples. Zones with a higher crack density are observed (Figures 8b to d) in most of the simulations, in what could be perceived as the onset of shear banding. Although some form of localisation occurs, no percolation takes place, since the different fractures fail to coalesce (Figures 8 and 11b). As the load is increased, further cracking may even obliterate the incipient shear banding that came to the foreground. The influence of the tessellation density on the response of the

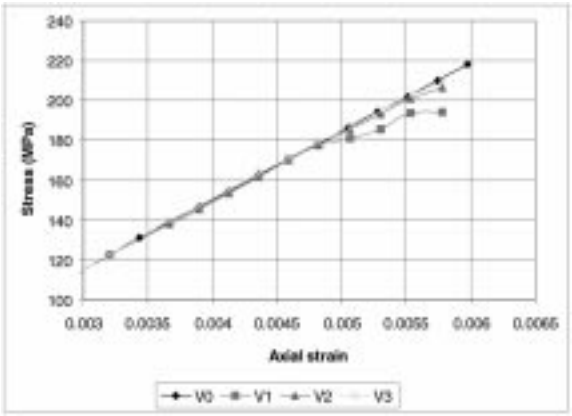

Figure 7. Average axial stress as a function of the average axial strain for the simultion of a biaxial test of a series of Voronoi samples with an increasingly higher tessellation density. The initial linear elastic part of the curve is omitted to focus on the non-linear part of the curve.

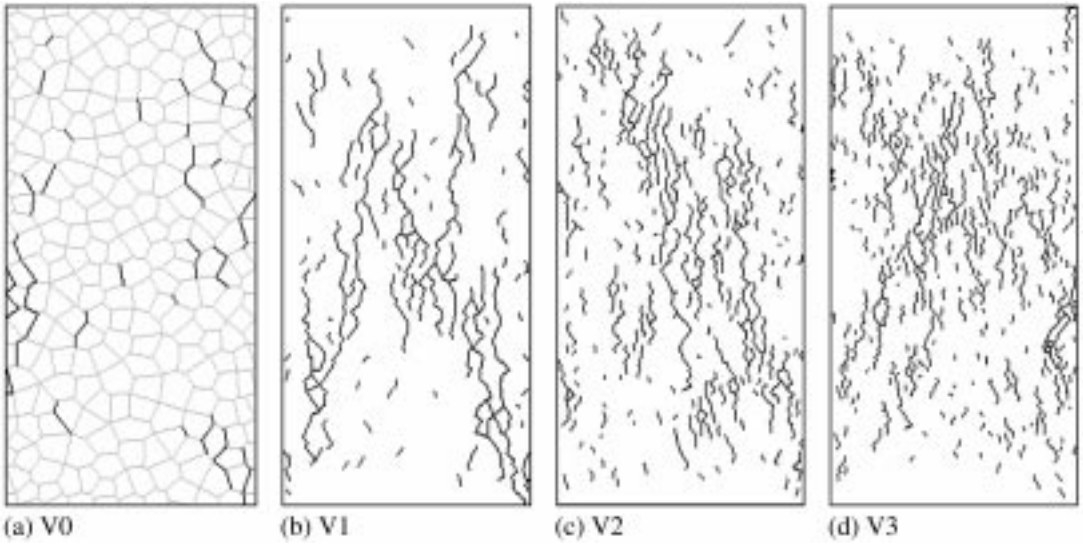

Figure 8. Fracture pattern obtained with an increasingly finer Voronoi tessellation at $\varepsilon = 0.006$ in the simulation of a biaxial test. The fracture pattern of V0 is overlaid on the tessellation pattern.
(a) V0. (b) V1. (c) V2. (d) V3.

samples remains in every sense very limited. Napier and Peirce (1995) studied the influence of the mesh size in samples meshed with Voronoi polygons not containing flaws on the simulation of UCS tests (Uniaxial Compressive Strength). Their investigation also indicated that the densely tessellated samples displayed almost no load shedding once failure is initiated. Based on their experiments and on the results obtained by Handley (1995), Napier and Peirce (1995) suggest that the Voronoi structure may be self-stabilising. These researchers also conducted some experiments with Voronoi patterns in which they allowed fracture initiation within the Voronoi polygons as well (Malan and Napier, 1994; Napier and Peirce, 1995). In such cases rapid load shedding is recorded.

The Voronoi tessellation with internal fracture paths was devised (Sellers and Napier, 1997) to investigate whether rapid load shedding could be obtained when fracturing is not confined

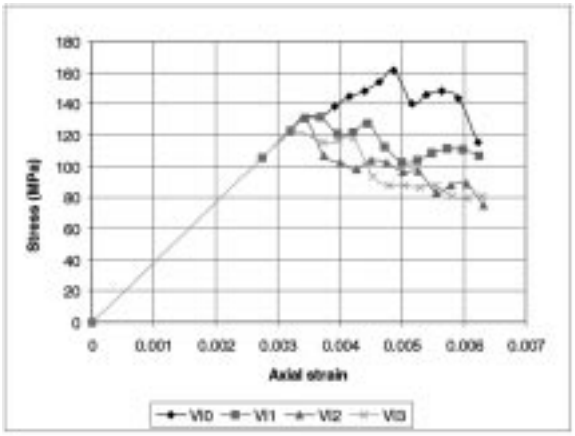

Figure 9. Average axial stress as a function of the average axial strain, for the simulation of a biaxial test of a series of Voronoi tessellations with internal fracture paths with an increasingly higher tessellation density.

to the Voronoi boundaries. The Voronoi polygons can be interpreted as the mineral grains, and the internal fracture paths as possible fracture paths within the grains that may have different strength properties than the grain boundaries. The samples meshed with Voronoi polygons with internal fracture paths contain 624 (VI0), 1764 (VI1), 3513 (VI2) and 7127 (VI3) elements. Mesh VI3 is obtained by adding internal fracture paths to Voronoi mesh V1. As for the Delaunay tessellation, the linear-elastic region and the non-linear region at the end of which the peak stress is reached, are also recognised in the stress-strain curves for the Voronoi tessellation with internal fracture paths (Figure 9). In the post-peak region, a more gentle stress decrease is recorded than in the Delaunay tessellation. As in the Delaunay tessellation, the brittleness can be increased by bringing the strength properties of the flaws and the intact elements closer together. The simulations in which a frictionless platen-sample contact is modelled exhibit again a more brittle behaviour. There is also a parallel with the Delaunay tessellation as far as the influence of the tessellation density on the localisation mechanism is concerned. In the densely meshed samples a shear band consisting of small coalescing fractures is formed (Figures 10 and 11c), while a few long fractures that form a shear plane dominate the fracture pattern in the coarser meshed samples (Figure 10). The shear banding is most pronounced in the samples with the most densely tessellated samples.

The Delaunay tessellation and the Voronoi tessellation with internal fracture paths generally show an improvement in the fracture pattern for increasingly finer tessellation patterns. A mean element size of approximately one thirtieth of the sample width (D2, Figure 6c; V2; Figure 8c and VI3, Figure 10d) seems to be sufficiently fine to satisfactorily simulate the fracturing process and the resulting fracture pattern. For a sample with a width of 50 mm, modelling at grain level would require a decrease in element size with a factor 10 to 20. This would result in a significant increase in the CPU-time and memory requirements (Peirce and Napier, 1995). Just as the flaws are equivalent structures for the defects in the material, the elements are equivalent structures for the intact material comprising cleavage planes and grain boundaries. Based on the results, the oversizing of the elements seems to be acceptable.

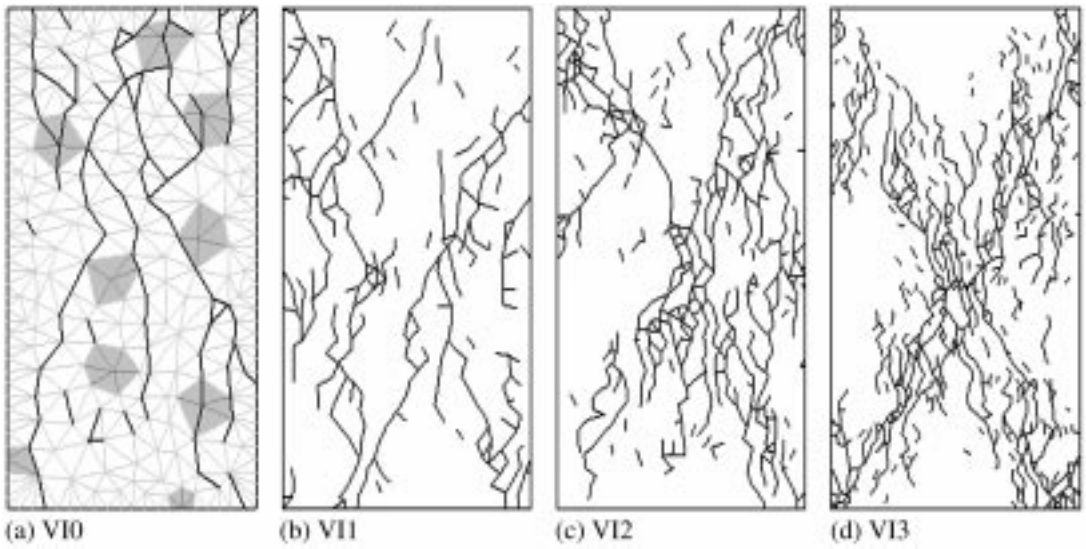

Figure 10. Fracture pattern obtained with an increasingly finer Voronoi tessellation with internal fracture paths at $\varepsilon = 0.0063$ in the simulation of a biaxial test. The fracture pattern of VI0 is overlaid on the tessellation pattern. A few of the polygons have been shaded, illustrating the difference between polygons and internal fracture paths.

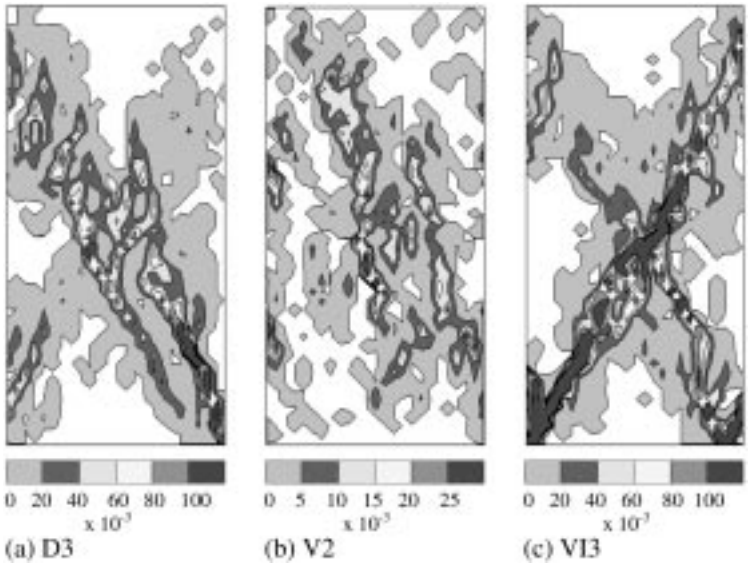

Figure 11. Octahedral inelastic shear strain associated with the fracture pattern depicted in Figure 6d (sample D3, Delaunay), Figure 8c (sample V2, Voronoi) and Figure 10d (sample VI3, Voronoi with internal fracture paths).

4.2. TESSELLATION PATTERN

A comparison of the stress-strain curves (Figures 5 and 9), the fracture pattern (Figures 6 and 10) and the octahedral inelastic shear strain (Figure 11) of the Delaunay tessellation and the Voronoi tessellation with internal fracture paths indicates that the response obtained for both tessellation patterns is qualitatively similar if comparable strength characteristics are used. The response of the Voronoi tessellation on the other hand differs radically from the response obtained with the two previous tessellation patterns and with the laboratory observations. The

reason for the similarity between the Delaunay and the Voronoi with internal fracture paths and the difference with the Voronoi is attributed to the number of potential fracture paths available at each node for fracture growth and coalescence. The number of potential fracture paths is approximately six in the case of the Delaunay tessellation and three in the case of the Voronoi tessellation.

A comparison between the characteristics of an unmodified Voronoi, a Delaunay and a Voronoi tessellation with internal fracture paths indicates that the element size distribution and the distribution of the angle between neighbouring elements of the former is different from the latter two. It can be shown that the stresses at the collocation point c_1' (Figure 1) closest to a crack tip increase if the size of an element is decreased in comparison to the size of a neighbouring crack. In samples with a large range in element sizes, the smaller elements adjacent to large elements are easily activated. They have however only a minor influence on the fracture pattern or the stress redistribution compared to the influence of their large neighbours. Hence, the fracture pattern in samples with a large range in element sizes is determined by the larger elements. The angle size distribution though is believed to be of major importance in explaining the difference in behaviour between the unmodified Voronoi tessellation and the other two tessellation patterns.

The angle characteristics for the three tessellation patterns under investigation are brought together in Table 3. The element angle distribution in the mesh obtained with a Voronoi tessellation with internal fracture paths is in fact built up of two sub-populations: the angles between the elements at the geometric centres, and the angles between the elements at the corners of the polygons. The characteristics of each of the sub-populations are therefore given as well.

The Delaunay tessellation and the Voronoi tessellation with internal fracture paths have similar angle distributions. Both distributions are characterised by a positive skewness, and the average number of elements per node is identical. The range of angles between elements and the standard deviation on the average angle are somewhat larger for the Voronoi tessellation with internal fracture paths than for the Delaunay tessellation (Table 3). The distribution of the element angle in the Voronoi tessellation differs markedly from the two other tessellation patterns. In a Delaunay or a Voronoi tessellation with internal fracture paths, the average number of elements per node is nearly twice the average number of elements per node in a Voronoi mesh. It has been shown that whether an element joined to a crack or a fracture is activated or not, depends mainly on the orientation of the element (see Figure 2). Fracture growth and fracture coalescence is therefore facilitated in the Delaunay tessellation and the Voronoi tessellation with internal fracture paths.

The self-stabilising effect in the Voronoi tessellation would disappear if additional fracture paths were available. The fracture density obtained at $\varepsilon = 0.0067$ in sample V2 (Figure 12) is not uniformly distributed over the sample. The pattern could be described as consisting of individual, subvertical fractures that are only sporadically interconnected. The areas of high density fracturing form a pair of conjugate shear bands. The subvertical fractures lead to the formation of apparently stable columns. A detail of such a column-like structure, overlaid on the Voronoi tessellation is given in Figure 12b. The polygons in between two such fractures are ‘piled’ on top of each other. The element forming the interface between two polygons in a column is nearly orthogonal to σ_{I} and is unlikely to be activated. Since no alternative fracture paths are available, coalescence cannot take place. The arrest of the fracture marked ‘a’ in Figure 12b is also due to a lack of element availability. To establish whether coalescence between the different fractures would occur if additional fracture paths were available,

Table 3. Characteristics of the angles formed at the nodes by the elements for different tessellation patterns.

	Delaunay	Voronoi	Voronoi with internal el.	Geometric centres	Corners polygons
Average number of elements at a node	6.0	3.3	6.0	5.2	6.5
Max. number of elements at a node	9	6	12	8	12
Most frequent number of elements at a node	6	3	6	5	6
Average angle between two neighbouring elements at a node	60°	110°	60°	69°	55°
Standard deviation	18.4°	21.6°	21.4°	26.9°	16.4°
Skewness	0.53	−0.36	0.56	−0.07	0.49
Min. angle	22°	43°	16°	20°	16°
Max. angle	126°	166°	136°	136°	123°
Number of angles	15267	13595	13734	4366	9368
Number of nodes	2544	4157	2278	842	1436

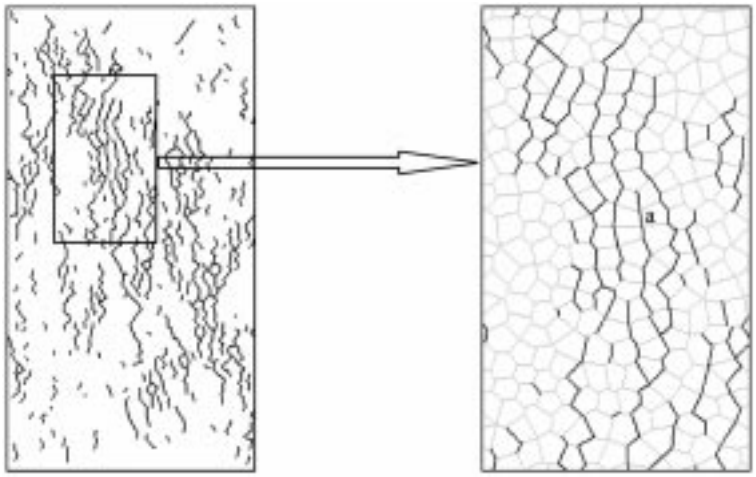

Figure 12. Fracture pattern obtained with a Voronoi tessellation (V2) at $\varepsilon = 0.0067$. (a) Vertical fractures concentrated in a diagonal band. (b) Detail of (a) overlaid on the tessellation.

a numerical experiment was carried out. Some additional elements, providing a connection between the different subvertical fractures, were added to the configuration depicted in Figure 12a. These additional elements are activated without having to increase the load, resulting in a coalescence of the existing fractures.

The limitation in the number of possible growth directions is not only reflected in the stress-strain curve. The percentage of elements activated under the same loading conditions, the average number of elements per fracture segment and the average length of the fracture segments also indicate that fracture growth is inhibited in the samples with a Voronoi mesh (Table 4). The fractures in a Delaunay tessellation grow at lower stresses, are longer and

3

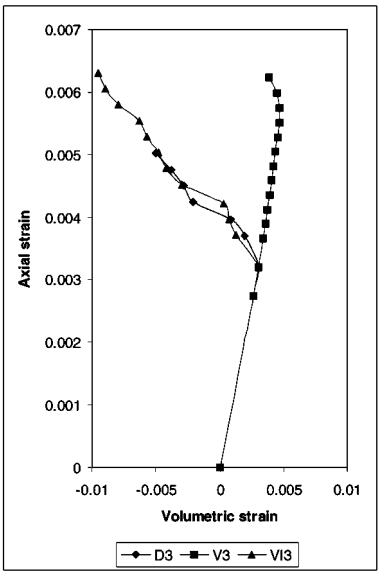

Figure 13. Comparison of axial strain against volumetric strain for Delaunay sample D3, Voronoi sample V3 and the sample with a Voronoi tessellation with internal fracture paths VI3. The octahedral inelastic shear strain at $\varepsilon = 0.00482$ is for the three samples respectively $\gamma = 10.81$ (D3), $\gamma = 0.30$ (V3), and $\gamma = 10.76$ (VI3).

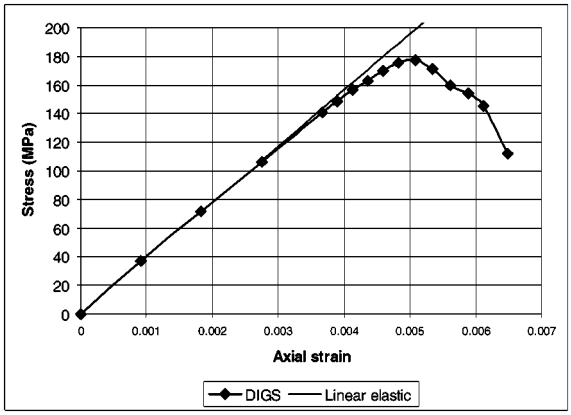

Figure 14. Average axial stress as a function of the average axial strain for the simulation of a biaxial test modelled with a Voronoi tesselation with internal fracture paths whereby the properties of the elements of the polygons and of the internal fracture paths have different values against a linear elastic response.

Table 4. Comparison of fracture characteristics of sample D2 and V2.

	Delaunay (D2)	Voronoi (V2)
% elements activated	7.6% ($\varepsilon = 0.0037$)	2.2% ($\varepsilon = 0.0037$)
Number of elements per fracture segment	4.1 (396 elements activated at $\varepsilon = 0.0037$)	2.3 (386 elements activated at $\varepsilon = 0.006$)
Ratio of average segment length to sample width	0.146 (total crack length 14.180 at $\varepsilon = 0.0037$)	0.077 (total crack length 13.460 at $\varepsilon = 0.006$)

contain more elements per fracture segment. The fracture segments are hereby defined as the parts of a fracture, which formed fractures in their own right before coalescence.

The difference in volumetric strain (Figure 13) between the Voronoi tessellation and the two alternative tessellation patterns is due to the restricted shear deformation as reflected by the average octahedral inelastic shear strain.

Although the Voronoi tessellation cannot reproduce the post-peak softening, the abundance of small individual fractures gives rise to a non-linear response corresponding to region III in Figure 4 ($\Delta\sigma_{ax}/\Delta\varepsilon_{ax} > 0$) in the stress-strain curves (Figure 7). In the Delaunay tessellation and the Voronoi tessellation with internal fracture paths on the other hand, the non-linearity before reaching the peak strength is, except for the coarsest tessellation, very limited or non-

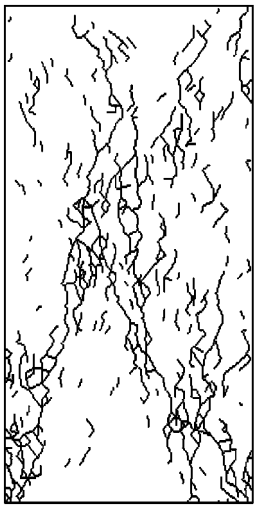

Figure 15. Fracture pattern obtained with a Voronoi tessellation with internal fracture paths at $\varepsilon = 0.006$, whereby the properties of the elements of the polygons and of the internal fracture paths have different values.

Table 5. Element and flaw properties used in the simulation of the biaxial test with different properties for the polygon elements and the internal fracture paths.

	Polygons		Internal fracture paths	
	Intact element	Flaw	Intact element	Flaw
Cohesion	80 MPa	25 MPa	160 MPa	50 MPa
Internal friction angle φ_i	35°	35°	35°	35°
Residual friction angle φ_r	20°	20°	20°	20°
Dilation angle ψ	15°	15°	15°	15°
Tension cut off	−35 MPa	−7 MPa	−70 MPa	−14 MPa

existent. Both features, the non-linear pre-peak response and the post-peak strain softening, can however be combined in the Voronoi tessellation with internal fracture paths. If the elements making up the polygons and the internal fracture paths are given different strength characteristics, both features can be reflected in one model. The cohesion and a tension cut off have therefore to be larger for the internal fracture paths than for the elements of the polygons (Table 5). The non-linear stress-strain response (Figure 14) is at first caused by the activation of flaws. As the stress further increases, the non-linearity is due to both the activation of flaws and the activation of an increasing number of polygon elements. As the peak strength is approached, the number of internal fracture paths that are activated becomes more important. This results in a fracture and crack coalescence (Figure 15) and a strain-softening response (Figure 14).

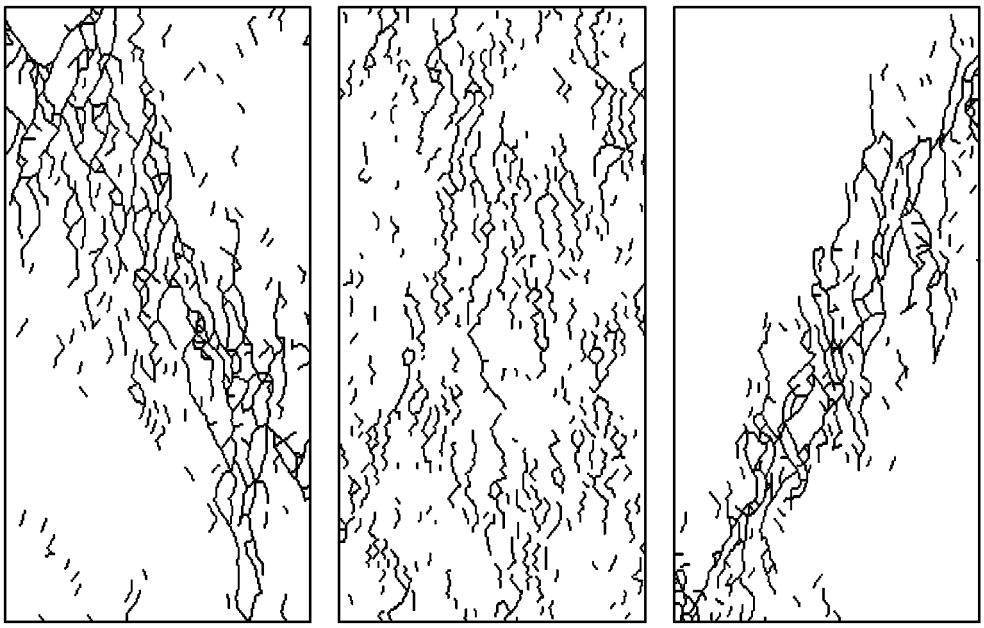

Figure 16. Fracture pattern obtained with a frictionless platen-sample contact for a Delaunay tessellation (Figure 16a, $\varepsilon = 0.0051$), a Voronoi tessellation (Figure 16b, $\varepsilon = 0.0072$) and a Voronoi tessellation with internal fracture paths (Figure 16c, $\varepsilon = 0.0051$).

4.3. SHEAR BAND FORMATION

In the simulations, at least three factors seem to play an important role in the formation of a shear band. Firstly, the general stress distribution in the sample, which is function of the applied stresses and boundary conditions, is important. It secondly appears that growing fractures are preferentially aligned in a shear band-like structure. The third factor pertains to the coalescence of the different cracks and fractures.

The fracture pattern in the Voronoi sample cannot be interpreted unambiguously (Figure 16b). In most of the Voronoi samples in which a frictional resistance was modelled between the sample and the platens (Figure 8b, 8c, and 8d), the larger fractures form a band-like structure. The lack of a clear and unequivocal alignment of the fractures in the sample with the Voronoi tessellation in which no friction is modelled indicates that the role of the general stress distribution induced by the applied boundary conditions cannot be ignored either. Note also that the activation of flaws near the platen is inhibited as a result of the additional confining stresses brought about by the frictional resistance. This is illustrated in for example the different fracture pattern near the platens in Figures 16b and 8d.

To demonstrate that the fractures and activated flaws can cause the stress redistribution favouring shear banding and that not only the stress state in the uncracked sample lies at the basis of the shear banding, a number of simulations were carried out with a frictionless sample-platen contact. The almost uniform stress distribution in these models does not inhibit flaw activation close to the platens and only the fractures and activated flaws can cause redistribution of the stresses. Shear banding is obtained in both the Delaunay and Voronoi tessellation with internal fracture paths (Figure 16). It is observed that a number of fractures and a number

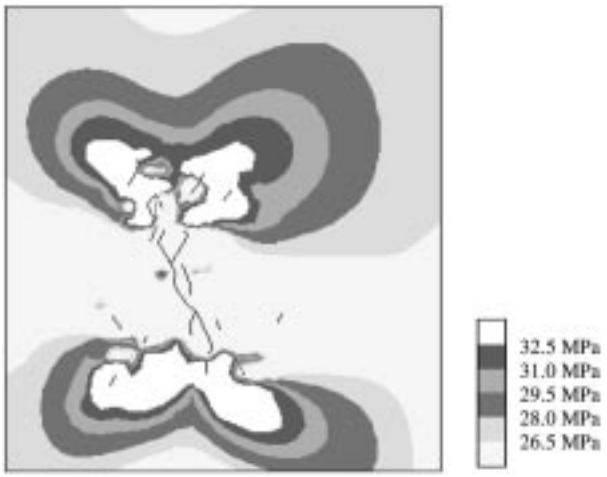

Figure 17. ESS-distribution around a set of 13 cracks and small fractures after 36 growth increments. The depicted area measures 50 mm × 55 mm and is part of a 50 mm × 100 mm sample ($\varepsilon = 0.00367$).

of activated flaws in their vicinity behave as a single structure. The stress redistribution around this structure favours fracture growth and crack activation in a shear band like structure. This is illustrated in Figure 17. It shows the stress distribution around a structure that consists of a total of 13 cracks and fractures placed in an otherwise uniform stress field. The stress distribution around this structure favours flaw activation and fracture growth at the top and the bottom of the structure in a direction inclined to the axial stress, while the region along the fracture is partially de-stressed. The resulting stress redistribution favours further crack activation and fracture growth in a shear band like direction.

It is generally recognised that crack-crack interaction can be complex and different types of coalescence patterns have been described. It has been recognised that the coalescence mechanisms are not only material related, but are also dependent on the geometry of the fractures involved in the process. Horii and Nemat-Nasser (1985), Ashby and Hallam (1986) and Li et al. (1998) demonstrate the importance of wing cracks. Other researchers associate particular crack patterns with a particular coalescence mechanism, involving wing cracks, shear failure or a combination of shear and tensile failure (Kranz, 1979b; Wong and Chau, 1998; Bobet and Einstein, 1998a, b). The coalescence mechanisms in the simulations are also a complicated process that starts shortly after the first fractures are generated and that carries on through the whole fracturing process. As may be derived from the discussions in the previous paragraphs, the availability of a sufficient number of fracture paths at each node is a necessary requirement to enable the individual fractures to coalesce such that localisation can take place. Besides the availability of suitably oriented elements, the orientation of the individual fractures, the stress redistribution caused by the presence of the cracks and fractures influence the coalescence process as well. Fractures that do not coalesce in a localisation process tend to grow in an axial direction (Figures 6, 8, 10, and 16c).

The inclination of the shear band from the direction of the major principal stress is for soils reported to be in the range between the Coulomb orientation (θ_C for a small shear band thickness and the Roscoe orientation (θ_R for larger shear band thickness (Vermeer, 1990). Arthur et al. (1977) provide experimental evidence that supports an intermediate orientation

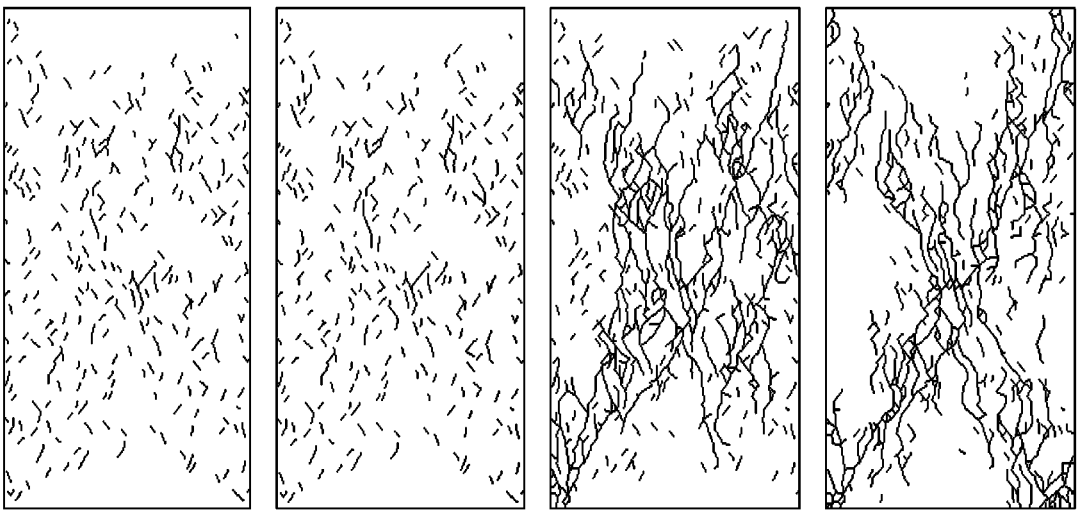

Figure 18. Influence of failure criterion and dilation on fracture pattern ($\varepsilon = 0.0061$). (a) Rankine criterion, $\psi = 0°$; (b) Rankine criterion, $\psi = 15°$; (c) Coulomb criterion, $\psi = 0°$; (d) Coulomb criterion, $\psi = 15°$.

θ_A:

$$\theta_C = 45° - \varphi_m/2, \tag{12}$$

$$\theta_R = 45° - \psi_m/2, \tag{13}$$

$$\theta_A = 45° - (\varphi_m + \psi_m)/4. \tag{14}$$

The friction angle φ_m and dilation angle ψ_m in (12), (13) and (14) are the 'macro' sample continuum values and have to be distinguished from values applicable to individual cracks (φ_i and φ_r for the friction angle and ψ for the dilation angle). The difference between the continuum values and the values on individual cracks is not unlike the difference noted between the friction angles of rocks and the friction angle of their individual constituting minerals (Jaeger and Cook, 1979). The forming of a shear band in the simulations is a rather complex mechanism whereby the inclination of the shear band is influenced by the internal friction angle, the residual friction angle, the confinement and the tessellation. The angle of the shear band in the simulations varies between 23° and 30° from the direction of the major principal stress. If it is assumed that $\varphi_m = \varphi_r$ and $\psi_m = \psi_i$, then $\theta_C = 27.5°$, $\theta_R = 37.5°$ and $\theta_A = 32.5°$. In additional simulations not shown here, the influence of the dilation angle and the combined influence of the friction angles φ_i and φ_r on the shear band inclination were tested. The influence of changes in the dilation angle on the shear band inclination is minimal. However, as the values of both φ_i and φ_r is altered, the inclination of the shear band angle changes as well, such that it corresponds more or less with the Coulomb orientation (Equation 12).

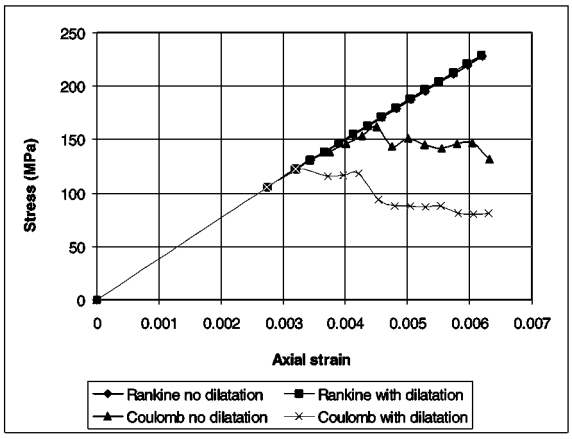

Figure 19. Average axial stress as a function of the average axial strain for the simulation of a biaxial test with a Rankine criterion, $\psi = 0°$; a Rankine criterion, $\psi = 15°$; a Coulomb criterion, $\psi = 0°$; and a Coulomb criterion, $\psi = 15°$.

4.4. FAILURE CRITERION

The tensile failure mode is often considered to be the basic failure mechanism (Hallbauer et al., 1973; Peng and Johnson, 1972; Sprunt and Brace, 1974; Kranz, 1979; Batzle et al., 1980; Blair and Cook, 1998). The extension and coalescence of these extensile cracks should then lead to macroscopic failure patterns such as shear banding. To determine whether this theory is applicable at the scale at which the material is modelled and for the way the defects are modelled, the fracture pattern obtained with simulations with a maximum-tensile-stress criterion (Rankine criterion) (Chen and Han, 1988) is compared to the pattern obtained with a Coulomb failure criterion.

The stress heterogeneity in a loaded rock is directly related to the heterogeneous nature of the material. Voids, variations in grain properties, the specific grain shape and mineral anisotropy amongst others can all be the source of a stress redistribution. All defects and all features causing a stress redistribution are modelled in the present study by means of displacement discontinuities. Since no tensile stresses are generated in a homogeneous sample subjected to a biaxial test, it is assumed that a population of pre-existing weaknesses (flaws) is present that can fail in shear. All the other elements are assumed to fail in tension only. The fracture pattern and the stress-strain curve obtained with a Rankine criterion for a sample meshed with a Voronoi tessellation with internal fracture paths is given in Figure 18a (dilation angle $\psi = 0°$). Cracking and fracturing are dispersed, and no clear localisation pattern appears. Since no shear planes are formed, no load shedding is observed either (Figure 19). To determine whether the dilation of activated flaws could lead to a localisation, the simulation was repeated with a dilation angle of $\psi = 15°$ (Figure 18b). The introduction of dilation has no marked influence on the fracture pattern and fracturing remains dispersed without localisation taking place. With the selected material properties and at the scale at which the simulations are carried out, a full Coulomb failure criterion is required to obtain localisation. The influence of the dilation on the response using a Coulomb criterion is illustrated as well (Figure 18c and 18d). The number of flaws activated before fracture growth and localisation commence is much higher when no dilation is introduced (Figure 18c). The peak stress is also higher in the simulation without dilation (Figure 19). As indicated in the discussion of

the stress distribution around individual cracks, the increase in the area of influence as well as the increase in stress levels that result from the increase in dilation angle favour fracture growth. Both the peak stress and the onset of the localisation process are hereby affected. The dilation is however not the driving force behind the localisation process, but only enhances the mechanisms that lay at the basis of fracture growth, coalescence and localisation.

The failure of the Rankine criterion to adequately represent the fracture and localisation process in the model can be traced back to the normal stress distribution in front of the crack tip as a function of the element angle β (Figures 1 and 2). As indicated before, the normal stress at the collocation point of elements joined to a crack as a function of the element angle β (Figures 1 and 2) goes through a minimum. The elements at which this minimum is recorded are approximately parallel to the major principal stress σ_{I}. It was further pointed out that, in a compressive stress field, the crack angle α must be large enough for the normal stress to be negative (= tensile). Since the normal stress is only negative for a small range in element angles that are more or less parallel to σ_{I} (Figure 2), the probability that a suitably oriented element is available at the crack tip is limited. If such an element is available and is activated, fracture growth occurs in a direction approximately parallel to the major principal stress σ_{I}. The newly activated element is however oriented in a direction subparallel to σ_{I}, a crack orientation for which the minimal normal stress at a distance c' in front of the crack tip tends to be positive in a compressive stress field. Further crack growth is therefore precluded. Hence, it can be concluded that in the model presented here the crack growth with a Rankine criterion is self-limiting.

5. Conclusions

A boundary element code with linear variation displacement discontinuity elements (DIGS) has been demonstrated to be able to model fracture initiation, fracture growth and localisation. Applied in combination with a tessellation approach, the models can take account of the granular composition, intragranular cleavage planes and the presence of material defects. The attention in this paper has been focussed on the simulation of biaxial tests on rock samples. The code and the modelling approach under discussion have also already been used in the quantification of stope fracture zone behaviour in deep level gold mines in both a homogeneous rock mass and in a rock mass with bedding planes (Napier et al., 1997). The study presented in this paper must be seen as part of the attempt to further develop this code to interpret and predict expected underground behaviour.

The study of the stress distribution in the vicinity of a displacement discontinuity element and the comparison with the stress distribution in the vicinity of a flat elliptic crack indicated that the displacement discontinuity elements are able to model flat cracks. The highest normal stress on elements joined to a sliding crack is noted for elements subparallel to the major principal stress. This can, also in biaxial tests, give rise to mode I extensile crack growth in the direction of the major principal stress. The direction of the principal stresses also determines the directions in which fracture growth, by means of shear failure, can be expected. The net driving shear stress reaches its highest values on elements that are oriented in a direction similar to the sliding crack and make an angle of approximately 25° with the major principal stress.

At the scale at which the material is modelled, both tensile and shear failure play a role. With a Rankine criterion, no localisation can be obtained. A full Coulomb failure criterion is

required to obtain the shear banding observed in laboratory tests. It is shown that with the used model, a pure tensile fracture is self-limiting: the direction in which the tensile fractures grow, preclude further mode I crack activation. A shear failure mechanism is therefore required to allow for continuing fracture growth and coalescence.

The numerical experiments to determine the influence of the mesh size and the tessellation type on the response showed that although some form of localisation occurs, the fractures fail to coalesce and no load shedding occurs in a sample meshed with a Voronoi tessellation. The Voronoi tessellation seems to be self-stabilising, and the response is not influenced by the tessellation density. The Voronoi tessellation with internal fracture paths and the Delaunay tessellation exhibit a strain softening behaviour and are characterised by a localisation of the deformation in shear bands. These two types of tessellations behave in a similar way. Increasing the tessellation density makes the shear banding more pronounced. The different response of the Voronoi tessellation on the one hand and the Delaunay and Voronoi tessellation with internal fracture paths on the other hand, can be explained by the higher number of possible fracture paths that are available at each node. The triangulations have an average co-ordination of approximately six elements per node, while the Voronoi tessellation has an average co-ordination of about 3.3 elements per node. This implies that the fracture growth and coalescence occurs more easily in the former resulting in the typical shear banding pattern encountered in biaxial tests. To take advantage of both the non-linear pre-peak response noted in the Voronoi tessellation, and to reproduce at the same time the peak strength and the post-peak softening, a Voronoi tessellation with internal fracture paths can be used, whereby the elements of the polygons and the internal fracture paths are assigned different strength properties.

It was further demonstrated that friction between the loading platens and the sample inhibits fracturing near the platen contact. The influence of the boundary conditions such as the sliding resistance at the contact between the loading platens and the sample has an influence on the general stress distribution in the sample. The frictional resistance at the platen contact seems to favour shear banding in especially the Voronoi samples. Shear banding does however occur in the Delaunay samples and in the Voronoi samples with internal fracture paths that are modelled with a frictionless platen contact. The activated flaws and the fractures themselves seem to cause a stress redistribution in the sample leading to crack activation in a localised, shear band like manner. The coalescence of small fractures proved to be of crucial importance in the localisation process. Further research is required to investigate to which extent the physical processes involved in coalescence can be represented in the numerical models.

References

Arthur, J.R.F., Dunstan, T., Al-Ani, Q.A.J.L. and Assadi, A. (1977). Plastic deformation and failure in granular media. *Géotechnique* **27**, 53–74.

Ashby, M.F. and Hallam, S.D. (1985). The failure of brittle solids containing small cracks under compressive states. *Acta Metallurgica* **34**, 497–510.

Bathurst, R.G.C. (1991). *Carbonate sediments and their diagenesis*, Elsevier, Amsterdam. 620 pp.

Batzle, M.L., Simmons, G. and Siegfried, R.W. (1980). Microcrack closure under stress: direct observation. *Journal of Geophysical Research* **85**, 7072–7090.

Blair, S.C. and Cook, N.G.W. (1998). Analysis of compressive fracture in rock using statistical techniques: Part I. A non-linear rule-based model. *International Journal of Rock Mechanics and Mining Sciences* **35**, 837–848.

Bobet, A. and Einstein, H.H. (1998a). Fracture coalescence in rock-type materials under uniaxial and biaxial compression. *International Journal of Rock Mechanics and Mining Sciences* **35**, 863–888.

Bobet, A. and Einstein, H.H. (1998b). Numerical modelling of fracture coalescence in a model rock material. *International Journal of Fracture* **92**, 221–252.

Brady, B.H.G. and Brown, E.T. (1993). *Rock Mechanics for Underground Mining*, Chapman & Hall, London, 571 pp.

Chen, W.F. and Han, D.J. (1988). *Plasticity for Structural Engineers*, Springer-Verlag, New York, 250 pp.

Chen, Y, Nishiyama, T., Kusuda, H., Kita, H. and Sato, T. (1999). Correlation between microcrack distribution patterns and granitic rock splitting planes. *International Journal of Rock Mechanics and Mining Sciences* **36**, 535–541.

Crawford, A.M. and Curran, J.H. (1982). Higher-order functional variation displacement discontinuity elements. *International Journal of Rock Mechanics and Mining Sciences* **19**, 143–148.

Crouch, S.L. and Starfield, A.M. (1983). *Boundary Elements in Solid Mechanics*, Allen & Unwin, London, 606 pp.

Finney, J.L. (1979). A procedure for the construction of Voronoi polyhedra. *Journal of Computational Physics* **32**, 137–143.

Hallbauer, D.K., Wagner, H. and Cook, N.G.W. (1973). Some observations concerning the microscopic and mechanical behaviour of quartzite specimens in stiff, triaxial compression tests. *International Journal of Rock Mechanics and Mining Sciences* **10**, 713–726.

Handley, M.F. (1995). *An investigation into the constitutive behaviour of brittle granular media by numerical experiment*, Ph.D. thesis, Univ. Minnesota, 314 pp.

Horii, H. and Nemat-Nasser, S. (1985). Compression induced microcrack growth in brittle solids: Axial splitting and shear failure. *Journal of Geophysical Research* **90**, 3105–3125.

Jaeger, J.C. and Cook, N.G.W. (1979). *Fundamentals of Rock Mechanics*, Chapman and Hall, London, 593 pp.

Kranz, R.L. (1979a). Crack growth and development during creep of Barre granite. *International Journal of Rock Mechanics and Mining Sciences* **16**, 23–36.

Kranz, R.L. (1979b). Crack-crack and crack-pore interactions in stressed granite. *International Journal of Rock Mechanics and Mining Sciences* **16**, 37–47.

Kožušnikova, A. and Marečkova, K. (1999). Analysis of rock failure after triaxial testing. *International Journal of Rock Mechanics and Mining Sciences* **36**, 243–251.

Kuijpers, J.S. and Napier, J.A.L. (1996). Effective growth rules for macrofracture simulation in brittle rock under compression. *Eurock'96* (edited by Barla, G.), Balkema, Rotterdam, 469–479.

Lawn, B. (1993). *Fracture of Brittle Solids*, Cambridge University Press, Cambridge, 378 pp.

Li, C., Prikryl, R. and Nordlund, E. (1998). The stress-strain behaviour of rock material related to fracture under compression. *Engineering Geology* **49**, 293–302.

Malan, D.F. and Napier, J.A.L. (1995). Computer modelling of granular material microfracturing. *Tectonophysics* **248**, 21–37.

Napier, J.A.L. (1990). Modelling of fracturing near deep level gold mine excavations using a displacement discontinuity approach. *Proceedings of the second international conference on mechanics of jointed and faulted rock* (edited by Rossmanith, H.-P.), Balkema, Rotterdam, 709–715.

Napier, J.A.L. and Hildyard, M.W. (1992). Simulation of fracture growth around openings in highly stressed brittle rock. *Journal of the South African Institute of Mining and Metallurgy* **92**, 159–168.

Napier, J.A.L. and Peirce, A.P. (1995). Simulation of extensive fracture formation and interaction in brittle materials. *Proceedings of the second international conference on mechanics of jointed and faulted rock* (edited by Rossmanith, H.-P.), Balkema, Rotterdam, 63–74.

Napier, J.A.L. and Malan, D.F. (1997). A viscoplastic discontinuum model of time-dependent fracture and seismicity effects in brittle rock. *International Journal of Rock Mechanics and Mining Sciences* **34**, 1075–1089.

Napier, J.A.L., Daehnke, A., Dede, T., Hildyard, M.W., Kuijpers, J.S., Malan, D.F., Sellers, E.J. and Turner, P.A. (1997). Quantification of stope fracture zone behaviour in deep level gold mines. *Journal of the South African Institute of Mining and Metallurgy* **97**, 119–134.

Peirce, A.P. and Napier, J.A.L. 1995. A spectral multipole method for efficient solution of large-scale boundary element models in elastostatics. *International Journal for Numerical Methods in Engineering* **38**, 4009–4034.

Peng, S.S. and Johnson, A.M. (1972). Crack growth and faulting in cylindrical specimens of Chelmsford granite. *International Journal of Rock Mechanics and Mining Sciences* **9**, 37–86.

Reeves, M.J. (1985). Rock surface roughness and frictional strength. *International Journal of Rock Mechanics and Mining Sciences* **22**, 429–442.

Sellers, E. and Napier, J. (1997). A comparative investigation of micro-flaw models for the simulation of brittle fracture in rock. *Computational Mechanics* **20**, 164–169.

Sprunt, E.S. and Brace, W.F. (1974). Direct observations of microcavities in crystalline rocks. *International Journal of Rock Mechanics and Mining Sciences* **11**, 139–150.

Vermeer, P.A. (1990). The orientation of shear bands in biaxial tests. *Géotechnique* **40**, 223–236.

Walsh, J.B. (1965a). The effect of cracks on the uniaxial elastic compression of rocks. *Journal of Geophysical Research* **70**, 399–411.

Walsh, J.B. (1965b). The effect of cracks on the compressibility of rock. *Journal of Geophysical Research* **70**, 381–389.

Wong, R.H.C. and Chau, K.T. (1998). Crack coalescence in a rock-like material containing two cracks. *International Journal of Rock Mechanics and Mining Sciences* **35**, 147–164.

Wong, T.-F. (1982). Micromechanics of faulting in Westerley granite. *International Journal of Rock Mechanics and Mining Sciences* **19**, 49–64.